Ceramics International 50 (2024) 24417–24424

Contents lists available at ScienceDirect

Ceramics International

journal homepage: www.elsevier.com/locate/ceramint

Molybdenum doped indium oxide thin films grown on mica substrates with high near-infrared transparency and electron mobility for flexible optoelectronic and spintronic applications

Jindong Liu

School of Physics and Electronic Information, Yantai University, Yantai, 264005, China

ARTICLE INFO

Handling Editor: Dr P. Vincenzini

Keywords:
Flexible electronics
Transparent conductors
Diluted magnetic semiconductors
Mica
High near-infrared transparency
High electron mobility

ABSTRACT

In the era of the artificial intelligence, flexible multifunctional films that combine optical transparency, electrical conductivity, and ferromagnetism are highly beneficial for many advanced applications. Herein, we fabricated a flexible magnetic transparent conductor molybdenum doped indium oxide (IMoO) thin film on a mica substrate using a pulsed laser deposition (PLD) technique. The valence states of Mo dopants were determined to be Mo^{4+} and Mo^{6+} by X-ray photoelectron spectroscopy (XPS) analysis. From the measured optical transmittance spectrum, average visible (Vis) and near-infrared (NIR) transmittance (T_{ave_Vis} and T_{ave_NIR}) values in IMoO film are calculated to be 85.9 % and 85.4 %, respectively. The IMoO film shows an electron mobility (μ_e) of around 113 $cm^2\ V^{-1}\ s^{-1}$ and a sheet resistance (R_s) of 69 Ω. We illustrate the benefits of Mo doping, which leads to increased NIR transparency and μ_e compared to commercially available tin-doped indium oxide (ITO). On the other hand, the IMoO film shows clear magnetic hysteretic behaviors at room temperature, indicating the presence of ferromagnetism. The main origin of the ferromagnetism is presumably attributed to the Mo^{4+} ions with an electronic configuration of 4 d^2. Bending cyclic tests reveal favourable mechanical durability and bending stability in the IMoO/mica films. Our systematic investigation demonstrates that IMoO film possesses a superior optoelectronic performance beyond ITO, Mn-doped indium oxide (IMnO), and Sn-Mn-codoped indium oxide (ITMnO), substantiating the potential of the IMoO/mica film as a high-performance transparent conductive magnetic material for flexible optoelectronic and spintronic applications.

1. Introduction

Recently, there has been heightened interests in searching for transparent conductor (TC) materials with a high charge mobility (μ) due to their extensive application in optoelectronics and high operational speed in electronic devices [1–3]. However, ITO, the most widely used commercial TC, exhibits a typical μ_e only around 50 $cm^2\ V^{-1}s^{-1}$ [4]. The reduced μ_e value in ITO is attributed to the pronounced ionized impurity scattering [4–6]. The strong orbital hybridization between the Sn and In 5s states close to the conduction band minimum (CBM) can markedly renormalize the band structure and increase the electron effective mass (m^*) [5]. Several novel TC materials have recently been developed, including metal nanowire (NW) composites, strongly correlated metals, and oxide/metal/oxide sandwich heterostructures, all of which have demonstrated promising optoelectronic performance [7–14]. However, these compounds typically show μ_e values ranging from 1 to 14 $cm^2\ V^{-1}\ s^{-1}$ [7–14]. Besides, TC materials transparent across the Vis and NIR spectra are highly desirable because of the demands of the photovoltaic industry [15]. The long-wavelength absorption edge in a TC always lies in the infrared region, represented by the screened plasma energy ($\hbar\omega_p$):

$$\hbar\omega_p = \hbar e\sqrt{\frac{1}{\varepsilon_r\varepsilon_0}}\sqrt{\frac{n}{m^*}}, \tag{1}$$

where $\hbar$ is the reduced Planck's constant, ω_p the screened plasma frequency, e the elementary charge, ε_0 the permittivity of free space, ε_r the relative permittivity of material, and n the carrier density [16]. On the other hand, the dc electrical conductivity (σ) in a relaxation-time approximation is given by

$$\sigma = \frac{1}{\rho} = ne\mu = \frac{ne^2\tau}{m^*}, \tag{2}$$

where ρ denotes the electrical resistivity and τ the relaxation time [16].

E-mail address: Jliu@ytu.edu.cn.

https://doi.org/10.1016/j.ceramint.2024.04.172
Received 7 March 2024; Received in revised form 3 April 2024; Accepted 15 April 2024
Available online 16 April 2024

For ITO, Sn doping leads to an increase of n and thus increasing $\hbar\omega_p$ value [4–6]. Correspondingly, the transmittance in the NIR region of ITO is much reduced [4–6].

Diluted magnetic semiconductor (DMS) was proposed as a newly-developed functional material based on the synergistic combination of electronic and magnetic properties, showing great potential to facilitate innovative changes of spintronic devices by simultaneously controlling the spin and charge degrees of freedom [17–26]. Among masses of semiconductors, indium oxide (IO) is considered as one of the most promising DMS hosts for its excellent optoelectronic performance [23–28]. IO-based DMSs like IMnO, ITMnO, and Cr-doped IO have been previously investigated, exhibiting room-temperature ferromagnetism [23–28]. Among these IO-based DMSs, ITMnO shows the optimal multifunctional properties such as enhanced room-temperature ferromagnetism, high Vis transmittance, and high σ value [28]. In ITMnO compound, the Sn dopants offer electrons and Mn dopants provide spins, respectively [25,28]. Due to the heavier doping and thus more scattering, lower μ_e value and NIR transmittance were observed in ITMnO, which significantly impedes its practical applications in high-speed spintronic devices and photovoltaic industry [20]. Therefore, it is a pressing requirement to design alternative magnetic dopants in IO that can achieve higher μ_e value and NIR transmittance.

Integrating **Equation (1)** and **(2)** into account, it is found that the doped IO can own an enhanced σ while maintaining a high NIR transparency via increasing the μ_e rather than the n [6]. Previous investigations showed that the IMoO thin film possesses a high μ_e and thus was considered as a promising n-type TC beyond ITO [5,6]. In contrast to ITO, the orbital hybridization between the resonant Mo 4 d and In 5s states is much weaker under the crystal symmetry of IO [5,6]. Consequently, the dispersion of the conduction band near the CBM and therefore the m^* are largely retained in IMoO, as schematically illustrated in Fig. 1a [5,6]. Moreover, both previous theoretical and experimental studies indicated that the IMoO film is ferromagnetic at room temperature [6,23]. As schematically presented in Fig. 1b, differing from the codoped cases such as ITMnO, both the spin and charge carriers in IMoO come from dopant Mo, resulting in less scattering. We can thus expect that IMoO might be an ideal material system that simultaneously possesses high σ and μ_e, transparency across the Vis and NIR region, and room-temperature ferromagnetism.

In recent years, the design and synthesis of flexible functional films have received intense attention due to its great application potential in the fields of portable electronic devices, wearable sensors, and the internet of things [29–40]. Among lots of fabrication strategies, the direct deposition of a film layer on an all-inorganic platelike mica substrate has aroused considerable interests due to the thermal stability and easy process [31–36]. The soft technology for the layer/mica membranes was previously illustrated in detail [36]. In addition, the oxide growth on mica is deemed as a kind of van der Waals epitaxy growth without dangling bonds between the film layer and substrate [31–36]. Consequently, the layer/mica films always show high mechanical robustness and bending stability [31–36].

In this article, we present the integration of IMoO thin films on mica substrates for flexible optoelectronic and spintronic applications. In general, DMS films with low levels of magnetic doping show significant potential for use in spintronic devices, as high levels of magnetic doping often lead to spinodal decomposition [17,20,41]. On the other hand, previous studies indicated that the IMoO thin films with low Mo concentrations exhibit a high μ_e value attributed to reduced impurity scattering [4]. Hence, we have chosen to deposit IMoO thin films with a low Mo concentration (approximately 1.2 at. %) for our research. The present work establishes IMoO/mica film as a unique ferromagnetic transparent conductive material system that can simultaneously exhibit a high μ_e and a low R_s, remarkable transparency across the Vis and NIR wavelength range, good bending stability, and room-temperature ferromagnetism. Our experimental results imply that the IMO/mica films can be developed as an ITO-alternative multifunctional material for flexible X-tronic applications [38].

2. Experimental

2.1. Growth of flexible IMoO/mica films

IMoO thin films were deposited on mechanically exfoliated fluorphlogopite mica (001) substrates via a PLD method using a KrF excimer laser ($\lambda_L = 248$ nm) at a repetition rate of 6 Hz. The ceramic target for the growth (IO: $MoO_3 = 96 : 4$ wt %) was prepared by a solid-state reaction method [42]. The attempted preparative variables in this work ranged in 400–600 °C for growth temperature and 0.7–3.0 μTorr for oxygen pressure.

2.2. Structural characterizations and physical property measurements

The crystal structure information of the thin films was obtained using a high-resolution X-ray diffraction (XRD) apparatus. The surface morphology of the films was examined by a commercial atomic force microscope (AFM). The thin film thickness was determined using a commercial stylus profilometer. High-resolution XPS spectra were measured using a monochromatic Al Kα X-ray source at a pass energy of 50 eV to study the Mo chemical states and composition. To remove the native oxides at the film surface, a sputter-cleaning process was conducted using an argon ion gun. The Mo XPS spectrum was charge-calibrated with respect to the carbon 1s peak at binding energy 284.5 eV. In this work, the Mo atomic fractions of the utilized samples were determined using high-resolution XPS analysis. To prepare flexible IMoO/mica flakes, the as-grown IMoO films, along with the mica substrate that supports them, were peeled from the bulk substrate using mechanical cleaving. The thickness of the remaining mica substrate was calculated by subtracting the thickness of the peeled mica layers, which was determined using Young's Double-slit interference technique. To investigate the mechanical durability of the IMoO thin films, a battery of bending cyclic test experiments were carried out. The mechanical bending strain (Bs) in a film layer was exerted by mechanically buckling the flexible IMoO/mica lamellas against a series of polypropylene (PP) molds with various radii of curvature [27]. The microstructure of the films after the bending cycle test was studied using a scanning electron microscopy (SEM). The ultraviolet (UV) – Vis – NIR transmittance measurements were carried out using a commercial spectrometer. All the transmittance spectra of the thin films were corrected by subtracting the signals from the mica substrate. The electronic transport properties of the thin films were determined by the Van der Pauw method. Magnetization measurements were performed using a Quantum Design superconducting quantum interference device (SQUID) magnetometer. All the magnetization data of the IMoO thin films were corrected by subtracting the magnetic signals from the mica substrate and the PP mold.

3. Results and discussion

3.1. Optimal growth condition analysis

The results for the samples grown under various conditions are summarized in Table 1. The samples grown at 400 °C have μ_e values of around 50 $cm^2\ V^{-1}\ s^{-1}$, which is likely due to significant surface scattering [27]. On the other hand, the samples grown at 600 °C show μ_e values ranging from 72.5 to 89.3 $cm^2\ V^{-1}\ s^{-1}$. However, no hysteresis curves are clearly observed for any of these samples. This lack of hysteresis is attributed to the oxidation of more 4 d^2 Mo^{4+} ions, which are responsible for ferromagnetism, into 4 d^0 Mo^{4+} ions. The sample grown in an atmosphere with 1.5 mTorr oxygen at 500 °C exhibits the largest μ_e value. This sample is more near-stoichiometric and has lower defect concentration compared to samples grown in atmospheres with 0.7 and 3.0 mTorr oxygen. Based on these findings, the optimal sample growth

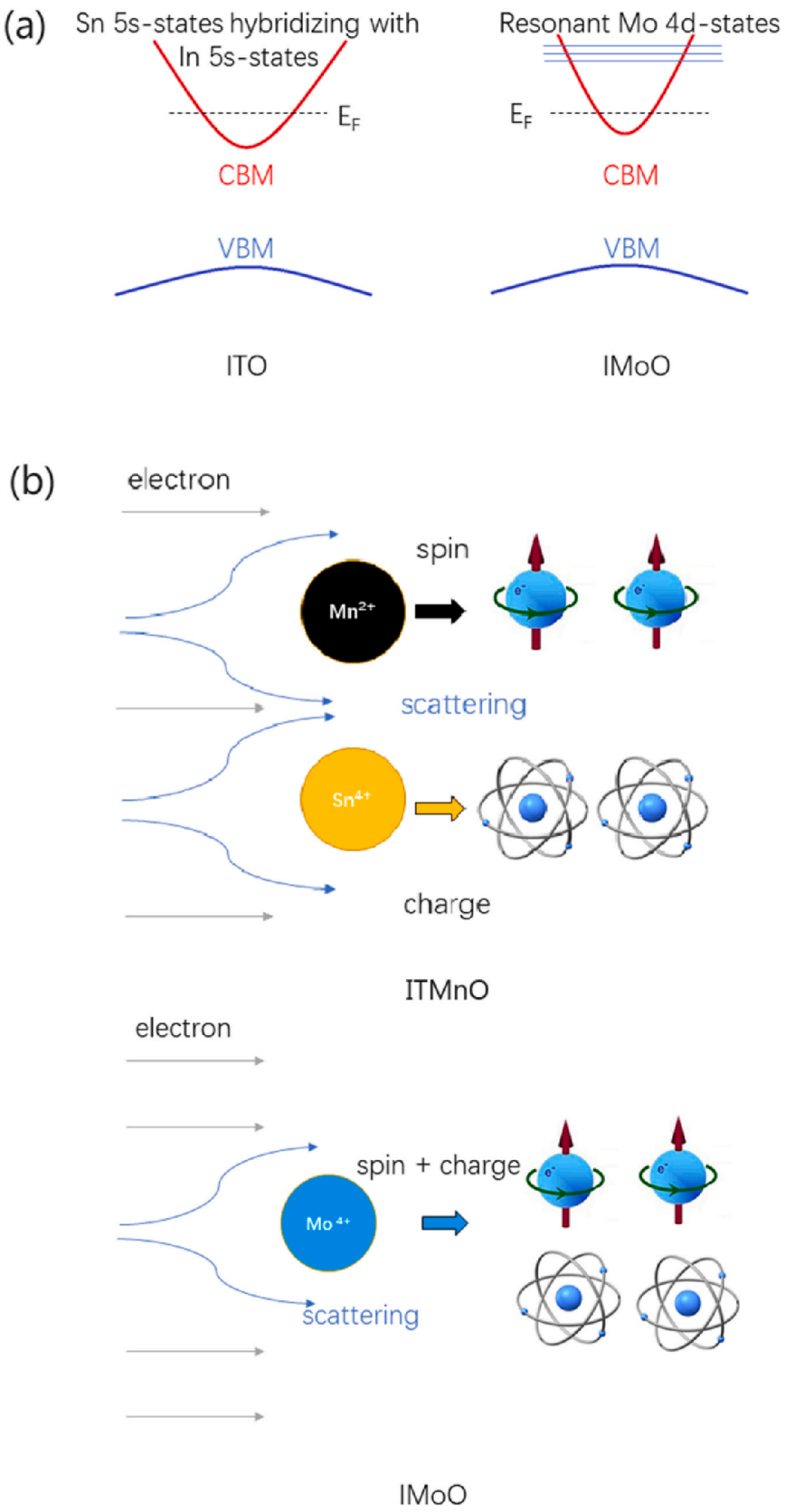

Fig. 1. (a) Schematic drawings of the dispersions of the band curvatures for the tin doped indium oxide (ITO) and the molybdenum doped indium oxide (IMoO). The Fermi level (E_F) is marked using dashed line. (b) Schematic diagram of the role of dopants on the spin and charge for Sn-Mn-codoped indium oxide (ITMnO) and IMoO.

Table 1
Experimental conditions and results of the investigated molybdenum doped indium oxide (IMoO) films[a].

T_g [°C]	$P(O_2)$ [mTorr]	Mo atomic fraction [at. %]	d [nm]	R_s [Ω/□]	μ_e [$cm^2 V^{-1} s^{-1}$]	T_{ave_Vis} [%]	T_{ave_NIR} [%]	FOM_{Vis} [$10^{-4}\Omega^{-1}$]	FOM_{NIR} [$10^{-4}\Omega^{-1}$]	M_s [emu/cc]	H_c [Oe]
400	0.7	1.5	90	141	44.3	87.3	86.2	18.2	16.1	4.9	300
400	1.5	1.5	85	136	48.7	88.0	86.9	20.5	18.1	5.1	300
400	3.0	1.6	90	118	50.6	86.6	85.1	20.1	16.9	5.4	250
500	0.7	1.4	100	84	95.0	82.9	80.5	18.3	13.6	4.8	280
500	1.5	1.2	100	69	113	85.9	85.4	31.5	29.8	4.4	355
500	3.0	1.1	105	91	88.9	87.1	86.8	27.6	26.7	3.9	200
600	0.7	2.2	110	39	86.7	77.8	65.0	20.8	3.5	–[b]	–[b]
600	1.5	2.1	110	42	72.5	78.4	67.3	12.1	4.5	–[b]	–[b]
600	3.0	1.9	115	55	89.3	80.1	69.6	19.8	4.8	–[b]	–[b]

[a] T_g, $P(O_2)$, d, R_s, μ_e, T_{ave_Vis}, T_{ave_NIR}, FOM_{Vis}, FOM_{NIR}, M_s, and H_c denote the growth temperature, oxygen atmosphere pressure, film thickness, sheet resistance, electron mobility, average transmittance in the visible region, average transmittance in the near-infrared region, figure of merit for the visible region, figure of merit for the near-infrared region, saturation magnetization, and coercive field, respectively.
[b] No hysteresis curves are clearly observed for these samples.

condition is determined to be a growth temperature of 500 °C in an atmosphere consisting of 1.5 mTorr oxygen. Hereinafter, our attention will be directed towards the samples grown under this optimal condition to further examine their structural and physical properties.

3.2. XRD and XPS analysis

Fig. 2 shows the θ-2θ XRD pattern of the IMoO thin film grown on a mica (001) substrate under the optimal growth condition. As can be seen from this pattern, all the diffraction peaks belonging to the IMoO film are relatively sharp, implying the high degree of texture of the film layers. Upon comparison with the XRD data of the bulk IO (JCPDS no. 88–2160, space group Ia3), the formation of a monophasic polycrystalline film layer with a cubic bixbyite-type structure was confirmed. A lattice constant of $a_{IMoO} = 10.073$ Å is determined from the Bragg peak position of (222) $_{IMoO}$, somewhat smaller than the bulk IO value ($a_{IO} = 10.118$ Å). Assuming that the Mo atoms substitute for the In atoms in the IO lattice, this is reasonable because the radii of the Mo ions ($R_{Mo3+} = 0.83$ Å, $R_{Mo4+} = 0.7$ Å, and $R_{Mo6+} = 0.62$ Å) are smaller than that of the In^{3+} ion ($R_{In3+} = 0.94$ Å) [43,44]. The average crystalline grain size (S_G) is estimated using Scherrer's equation

$$S_G = \frac{0.94\lambda_X}{\beta \cos\theta}, \quad (3)$$

in which λ_X is the X-ray wavelength ($\lambda_X = 1.5406$ Å), β the full width at half-maximum of the Bragg peak position of (222), and θ the diffraction angle [45]. From **Equation (3)**, a value of $S_G = 23.9$ nm is calculated for the peak (222) $_{IMoO}$. The inset in Fig. 2 shows the AFM image of the IMoO thin film. It is evident from the image that the surface of the IMoO film is continuous and uniform. The root-mean-square (RMS) roughness value is remarkably low at 1.26 nm, implying a potential reduction in surface scattering.

To determine the Mo chemical states and composition in the film layer, XPS analysis was undertaken. Fig. 3 exhibits the core-level XPS spectrum of the sample in the Mo 3 d region. As shown in Fig. 3, the dots represent experimental raw data points and the solid lines show our fits to the XPS data using a mixed Gaussian-Lorentzian peak function after the Shirley background subtraction [46]. According to our best fitting results, two contributions due to different valence states were identified: the Mo^{4+} component at the lower binding energy (purple curve) and the Mo^{6+} one at the higher binding energy (cyan curve) [46]. The red curve in Fig. 3 is the sum of these two Mo components, in good coincidence with the experimental raw data. The Mo^{4+} and Mo^{6+} component fractions as determined by our XPS fitting results are 26.2 % (2.1×10^{20} cm^{-3}) and 73.8 % (5.9×10^{20} cm^{-3}), respectively.

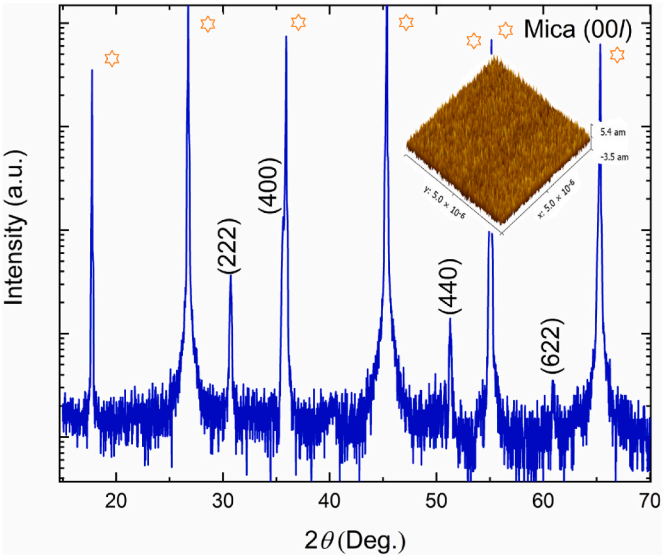

Fig. 2. θ–2θ X-ray diffraction (XRD) scan of the IMoO thin film grown on a mica substrate. Inset: Atomic force microscope (AFM) image (5 × 5 μm) of the IMoO film.

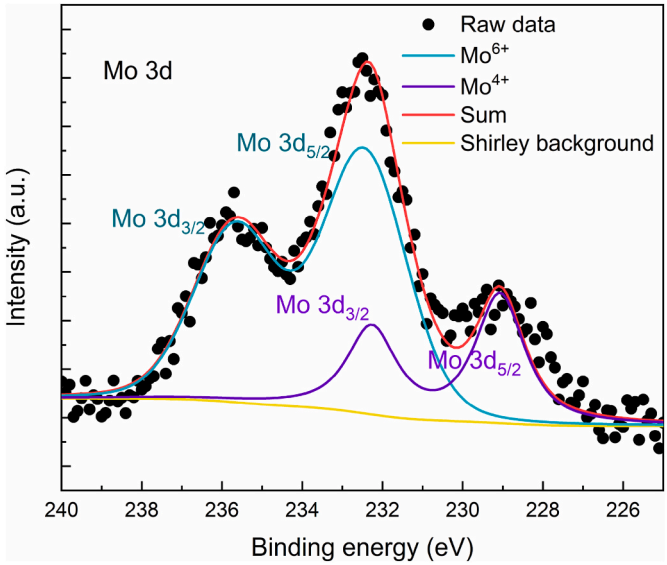

Fig. 3. Mo 3 d core level X-ray photoelectron spectroscopy (XPS) spectrum of the IMoO thin film.

3.3. Optical properties

We measured the normal incidence UV–Vis–NIR transmittance spectrum of a pristine IMoO film without bending, as indicated by the blue curve in Fig. 4. As can be seen from this curve, the IMoO film shows a high optical transmittance across the Vis and NIR wavelength range. The T_{ave_Vis} and T_{ave_NIR} values of the sample are calculated to be around 85.9 % and 85.4 %, respectively. The transmittance spectrum of a 100-nm-thick ITO film grown on a mica substrate was presented in Fig. 4 as well. Upon comparison between the transmittance spectra of the IMoO and the ITO film, we find that the IMoO film exhibits a much better optical transparency performance than the ITO film in the NIR region. The attenuated transparency of the ITO in the NIR region is ascribed to the increased n value (2.2×10^{20} cm^{-3}) and thus increased free-carried absorption [16]. In contrast, the n value of the IMoO film is around 8×10^{19} cm^{-3}, which ensures a high NIR transparency in the film layer.

In order to analyze the bandgap information, the Tauc plots for direct transitions constructed from the transmittance spectra (presented in Fig. 4) were shown in the inset in Fig. 4 [47]. According to Tauc's equation, the bandgap (E_g) values of IMoO [E_g (IMoO) = 3.85 eV] and ITO [E_g (ITO) = 3.52 eV] are obtained from the photon energy ($\hbar\upsilon$) axis intercepts [47]. IMoO shows larger E_g value than ITO, attributed to the smaller Burstein-Moss shift that governs optical absorption in the short-wavelength range [6,16]. From this data, we conclude that IMoO has better transparency than ITO in both the long and short wavelength ranges.

To investigate the mechanical durability of the flexible IMoO/mica film, the optical transmittance spectra of the sample undergoing bending cyclic tests were measured. The bending strain (Bs), applied by inflecting an IMoO/mica membrane using a given bending radius value (r) of curvature, is estimated by

$$Bs = \frac{t}{r}, \tag{4}$$

where t is the half thickness of the mica's residual layer, which was determined to be around 15 μm using Young's Double-slit interference technique [32]. In this work, a positive Bs value indicates a tensile bending whereas a negative one indicates a compressive bending. As for a flat film, Bs is assigned as zero value. We show the transmittance spectrum of a flexible IMoO/mica film bent for 10,000 times under a Bs = + 0.25 % in Fig. 4 as well. As can be observed from Fig. 4, the IMoO/mica film shows approximately same transmittance spectrum as the pristine one even after bent for 10,000 times, revealing a high bending stability in the ductile IMoO film.

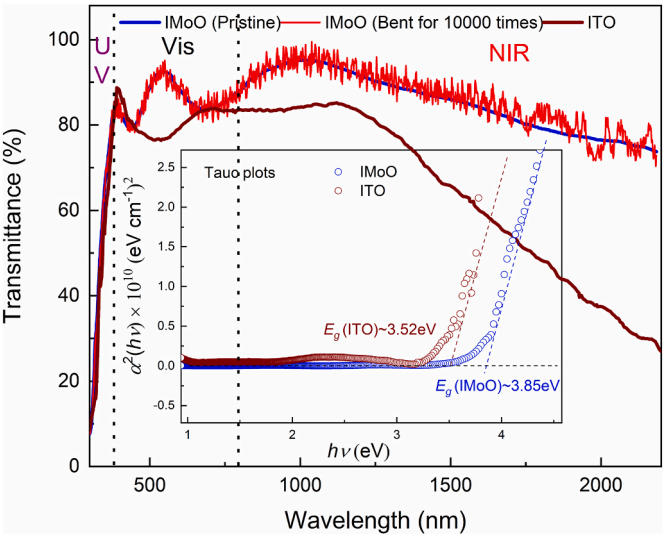

Fig. 4. Ultraviolet (UV) – visible (Vis) – near-infrared (NIR) transmittance spectra of the pristine IMoO/mica film that has never been bent (blue curve), the IMoO/mica film that has been bent for 10,000 times under a bending strain (B_s) of +0.25 % (red curve), and the pristine ITO/mica film (wine curve). Inset: Tauc plots of the IMoO and ITO films. (For interpretation of the references to colour in this figure legend, the reader is referred to the Web version of this article.)

3.4. Electrical characterizations

From the electrical measurements, the pristine IMoO/mica film shows a μ_e around 113 cm^2 V^{-1} s^{-1} and a R_s of 69 Ω at room temperature. Furthermore, a range of bending cycling tests were conducted to evaluate the electromechanical robustness and operational bending stability in flexible IMoO films. We measured the sheet resistance variance ($\Delta R_s/R_s$) following the bending of the samples under a given Bs value and present the $\Delta R_s/R_s$ as a function of Bs in Fig. 5a. In this article, the absolute values of the applied tensile (Bs_{cr_t}) and compressive Bs (Bs_{cr_c}) where the $\Delta R_s/R_s$ of the sample ascends to 5 % are employed to quantitatively depict the electromechanical robustness of flexible films. As can be found from Fig. 5a, with the applied tensile (compressive) Bs exceeding $Bs_{cr\_t} = 0.35$ % ($Bs_{cr\_c} = 0.46$ %), $\Delta R_s/R_s$ explosively increases with increasing Bs, implying the onset of cracking in the film layers. Notably, larger critical Bs value is found for the compressive case compared with the tensile case, in line with most flexible films [27,28,31,33,35]. Correspondingly, the critical bending radii (r_{cr}) are respectively 4.3 mm for the tensile film layers and 3.3 mm for the compressive ones, indicating a favourable electromechanical robustness in IMoO/mica film.

The bending stability of the IMoO/mica film was assessed by measuring the $\Delta R_s/R_s$ as a function of bending cycles and time under various Bs values, as shown in the insets in Fig. 5a. As can be seen from the upper inset in Fig. 5a, for the sample going through the bending cyclic tests with an applied Bs of +0.3 % (-0.43 %), which is lower than Bs_{cr_t} (Bs_{cr_c}), the $\Delta R_s/R_s$ ratio maintains lower than 5 % up to 10,000 bending cycles. Similar bending test results were also observed for the samples under applied Bs smaller than Bs_{cr_t} (Bs_{cr_c}). On the other hand, the lower inset in Fig. 5a shows that the $\Delta R_s/R_s$ values in the samples under applied tensile (compressive) Bs smaller than Bs_{cr_t} (Bs_{cr_c}) remain lower than 5 % for a long duration up to 10,000 s. To analyze the surface morphology of the samples following bending cyclic tests, SEM images of the IMoO films after 1000 bending cycles with applied Bs values of +0.3 % and +0.5 % are presented in Fig. 5b and c, respectively. The sample subjected to a Bs of +0.3 %, below Bs_{cr_t}, exhibits a smooth surface morphology free of any fractures. In contrast, the sample exposed to a tensile Bs of +0.5 % (exceeding Bs_{cr_t}) displays a clear rupture in the film layer, indicating a potential decrease in the electrical conductivity. These observations from the SEM analysis align with the $\Delta R_s/R_s$ results. These bending cyclic test results indicate exceptional electromechanical robustness and operational bending stability in flexible IMoO/mica films.

3.5. Magnetic behaviors

To determine the magnetic properties of the IMoO films, we present the magnetization versus applied magnetic field (M vs H) curve of the one measured at a temperature of 300 K in Fig. 6a. The measured sample shows a clear hysteretic behavior with a saturation magnetization (M_s) of 4.4 emu/cc and a coercive field (H_c) of ~355 Oe, indicating the presence of the room-temperature ferromagnetism in IMoO films. According to the aforementioned XPS analysis results, the concentration of Mo^{4+} ions with an electronic configuration of 4 d^2 is around 2.1×10^{20} cm^{-3}. Assuming that all the magnetic moments are provoked by the 4 d^2 Mo^{4+}, a theoretical M_s of 3.9 emu/cc is estimated. The experimental M_s value is slightly larger than the theoretical value, which is possibly related to the presence of oxygen defects in the lattice. Even though the discrepancy between the theoretical and experimental results exists, we

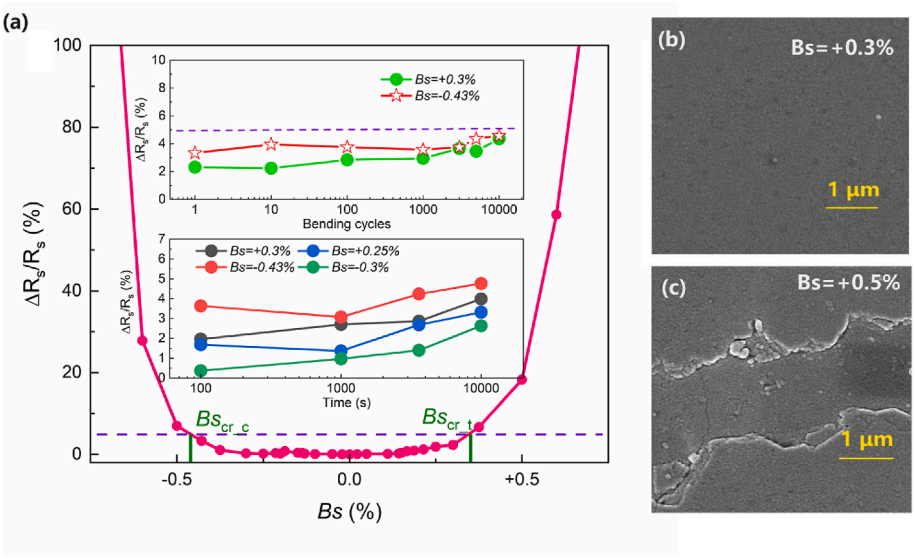

Fig. 5. (a) Sheet resistance variance ($\Delta R_s/R_s$) in IMoO/mica films as a function of *Bs* following the bending of the samples. Insets: $\Delta R_s/R_s$ plotted against (upper) bending cycles and (lower) time for the flexible IMoO/mica films under various tensile and compressive *Bs*. Scanning electron microscopy (SEM) images of the IMoO films after 1000 bending cycles with an applied *Bs* of (b) +0.3 % and (c) +0.5 %.

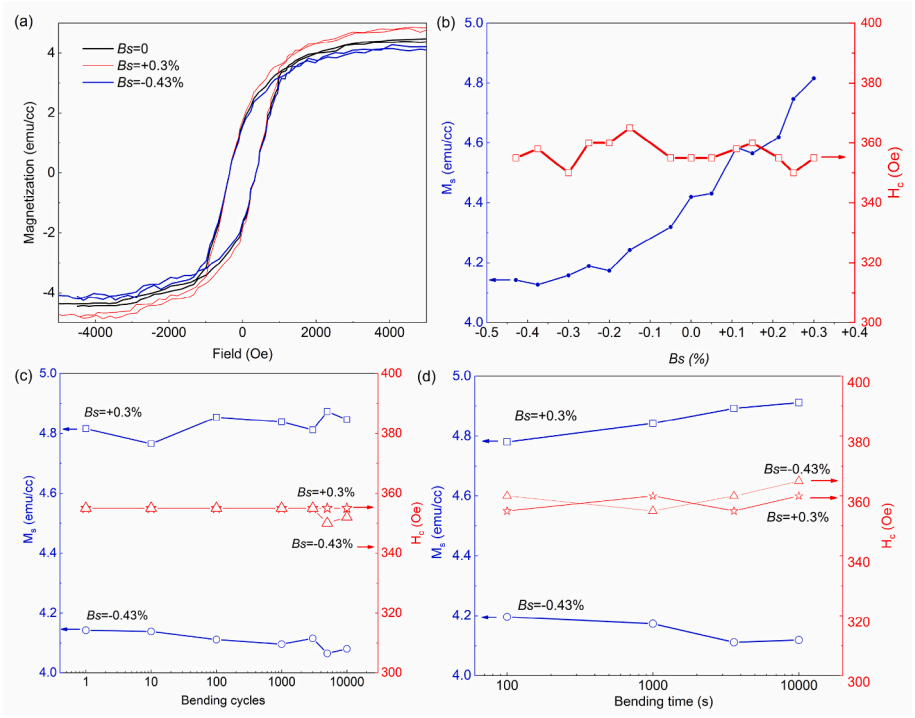

Fig. 6. (a) Magnetic hysteresis loops of the IMoO films under zero (*Bs* = 0 %), tensile (*Bs* = + 0.3 %), and compressive (*Bs* = - 0.43 %) *Bs* at 300 K. Saturation magnetization (M_s) and coercive field (H_c) values plotted against (b) *Bs*, (c) bending cycles, and (d) bending time.

presumably attributed the main origin of the room-temperature ferromagnetism to the Mo^{4+} ions.

To explore the operational bending stability of IMoO/mica films for flexible spintronic applications, we measured *M* vs *H* curves of the IMoO films under both tensile and compressive *Bs*. In the magnetization measurements, the magnetic field was applied parallel to the film plane and perpendicular to the *Bs* direction. The hysteresis curves of the samples under *Bs* values of both +0.3 % and −0.43 % were shown in Fig. 6a as well. On comparison among the three *M* vs *H* curves in Fig. 6a, it is found that all the three curves show similar hysteresis shapes and H_c values. Whereas, the M_s value increases (decreases) on applying a tensile (compressive) *Bs* of +0.3 % (-0.43 %). To investigate the dependence of the magnetic behaviors of flexible IMoO films on applied *Bs* in detail, we show the M_s and H_c values extracted from the measured *M* vs *H* curves as functions of *Bs* in Fig. 6b. As shown in Fig. 6b, the H_c value keeps at around 355 Oe within the experimental uncertainty, irrespective of whether the applied *Bs* is tensile or compressive. In contrast, the M_s value decreases from 4.4 emu/cc (*Bs* = 0) to 4.14 emu/cc (*Bs* = −0.43 %) with increasing compressive *Bs*, whereas it increases to 4.82 emu/cc (*Bs* = +0.3 %) with increasing tensile *Bs*.

The M_s and H_c values of the IMoO films under both tensile (Bs = +0.3 %) and compressive (Bs = −0.43 %) Bs plotted against bending cycles and time are displayed in Fig. 6c and d, respectively. From the four plots in Fig. 6c, both the M_s and H_c values are primarily preserved even up to 10,000 bending cycles. On the other hand, the four curves in Fig. 6d indicate that the H_c value is almost unchanged for a bending duration up to 10,000 s while the M_s value slightly increases (decreases) with bending time for the tensile (compressive) case. The systematic bending cyclic tests in conjunction with magnetization measurements reveal that the IMoO/mica film possesses excellent mechanical robustness and operational bending stability for flexible spintronic applications.

3.6. Comparison with flexible ITO, IMnO, and ITMnO films grown on mica substrates

In order to perform a multiperspective comparison in flexible IMoO (100-nm-thick), ITO (100-nm-thick), IMnO (140-nm-thick), and ITMnO (80-nm-thick) films grown on mica substrates, we make use of a histogram (Fig. 7) showing the optical, charge transport, and magnetic properties for these films [27,28]. As seen from Fig. 7a, IMoO film shows a much higher μ_e than the any other three flexible TC films, indicating an immense potential in the application of high-speed electronic devices. Moverover, IMoO film has a R_s of 69 Ω, which is lower than that of IMnO and comparable to those of ITO and ITMnO. As for the optical transparency in Vis wavelength range, IMoO film possesses a highest T_{ave_Vis} value amongst the four film layers, as shown in Fig. 7b. The Haacke figure of merit (FOM_{Vis}) is generally utilized to assess the performance of a film layer as a TC, defined by [48].

$$FOM_{Vis} = \frac{T_{ave\_Vis}{}^{10}}{R_s}. \quad (5)$$

The largest FOM_{Vis} value among the four TC films is also found in IMoO. To comprehensively evaluate the transparency in NIR wavelength range and the ability to conduct electricity, the figure of merit (FOM_{NIR}) for NIR region is proposed in this work, defined by

$$FOM_{NIR} = \frac{T_{ave\_NIR}{}^{10}}{R_s}. \quad (6)$$

As shown in Fig. 7c, an FOM_{NIR} of 2.98 × 10^{-3} Ω^{-1} is obtained for IMoO film, which is at least one order of magnitude larger than those for the other three samples, revealing the decided advantages of IMoO films in the NIR transparency over its opponents. As for the magnetic properties, the IMoO film possesses a comparable H_c value to IMnO and ITMnO, indicating stabilization of the room-temperature ferromagnetism in IMoO film layer.

4. Conclusions

In this study, a flexible IMoO/mica thin film was synthesized and experimentally confirmed as a high-performance transparent conductive magnetic material with high NIR transparency and μ_e. The μ_e value of IMoO is more than double as compared to that of ITO. On the other hand, both the T_{ave_Vis} and T_{ave_NIR} values in IMoO film are larger than the corresponding values in ITO film. Remarkably, the FOM_{NIR} value of the IMoO film is as high as 2.98 × 10^{-3} Ω^{-1}, which is about two order of magnitude larger than that of ITO. Moreover, room-temperature ferromagnetism was confirmed in IMoO film and the origin of the ferromagnetism is presumably ascribed to the 4 d^2 Mo^{4+} ions. Bending cyclic tests in conjunction with physical property characterizations reveal favourable mechanical durability and bending stability in IMoO/mica films. Our experimental results indicate that the IMoO/mica film has a superior optoelectronic performance beyond commercial ITO, demonstrating the significant potential of the IMoO/mica film as a high-performance transparent conductive magnetic material for flexible optoelectronic and spintronic applications.

CRediT authorship contribution statement

Jindong Liu: Conceptualization, Data curation, Formal analysis, Funding acquisition, Investigation, Methodology, Supervision, Writing – original draft, Writing – review & editing.

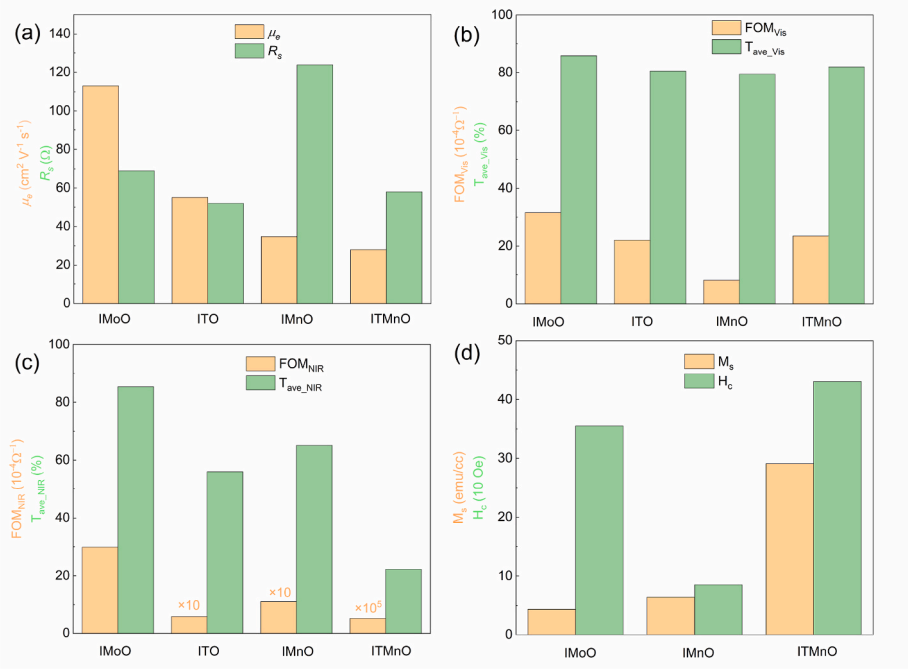

Fig. 7. Histogram displaying a multidimensional comparison in flexible IMoO, ITO, IMnO, and ITMnO films grown on mica substrates. (a) Presents electron mobility (μ_e) and sheet resistance (R_s), (b) presents Haacke figure of merit (FOM_{Vis}) and average transmittance (T_{ave_Vis}) for Vis region, (c) presents figure of merit (FOM_{NIR}) and average transmittance (T_{ave_NIR}) for NIR region, and (d) presents M_s and H_c extracted from room-temperature magnetic hysteresis loops.

Declaration of competing interest

All authors declare that no conflicts of interest exist.

Acknowledgment

This work was supported by the National Natural Science Foundation of China (Grant No. 61704081), the Natural Science Foundation of Shandong Province of China (Grant No. ZR2022MF290), the Natural Science Foundation of Jiangsu Province of China (Grant No. BK20170811), the China Postdoctoral Science Foundation (Grant No. 2016M601803), the Postdoctoral Science Foundation of Jiangsu Province (Grant No. 1701105C), and Yantai University (Grant No. WL20B71).

References

[1] R.A. Afre, N. Sharma, M. Sharon, M. Sharon, Transparent conducting oxide films for various applications: a review, Rev. Adv. Mater. Sci. 53 (2018) 79–89.
[2] K. McLellan, Y. Yoon, S.N. Leung, S.H. Ko, Recent progress in transparent conductors based on nanomaterials: advancements and challenges, Adv. Mater. Technol. 5 (2020) 1900939.
[3] J.M. Ribeiro, F.C. Correia, F.J. Rodrigues, J.S. Reparaz, A.R. Goñi, C.J. Tavares, Transparent niobium-doped titanium dioxide thin films with high Seebeck coefficient for thermoelectric applications, Surf. Coating. Technol. 425 (2021) 127724.
[4] D.S. Bhachu, D.O. Scanlon, G. Sankar, T.D. Veal, R.G. Egdell, G. Cibin, A.J. Dent, C. E. Knapp, C.J. Carmalt, I.P. Parkin, The origin of high mobility in molybdenum doped indium oxide, Chem. Mater. 27 (2015) 2788–2796.
[5] J. Xu, J.-B. Liu, B.-X. Liu, S.-N. Li, S.-H. Wei, B. Huang, Design of n-type transparent conducting oxides: the case of transition metal doping in In_2O_3, Adv. Electron Mater. 4 (2018) 1700553.
[6] J.E. Medvedeva, Magnetically mediated transparent conductors: in_2O_3 doped with Mo, Phys. Rev. Lett. 97 (2006) 086401.
[7] S. Yu, X. Liu, P. Yang, L. Zhao, H. Dong, C. Wu, X. Li, J. Xiong, Highly stable silver nanowire networks with tin oxide shells for freestanding transparent conductive nanomembranes through all solution processes, Chem. Eng. J. 446 (2022) 137481.
[8] S. Yu, P. Yang, B. Wang, N. Zhang, C. Wu, High-temperature resistance of flexible transparent conductive films based on Ag@ SnO_2 core-shell nanowires for 300° C, Mater. Lett. 328 (2022) 133031.
[9] H. Dong, S. Yu, L. Song, X. Wang, C. Wu, Fabrication of high-quality flexible transparent conductive thin films with a Nb_2O_5/AgNWs/Nb_2O_5 sandwich structure, Ceram. Int. 48 (2022) 15348–15354.
[10] S. Yu, X. Liu, H. Dong, X. Wang, L. Li, Flexible high-performance SnO_2/AgNWs bilayer transparent conductors for flexible transparent heater applications, Ceram. Int. 47 (2021) 20379–20386.
[11] J. Liu, All-inorganic flexible epitaxial $SrNbO_3$/mica thin films with ultrahigh figure of merit as indium-free transparent conductors, Ceram. Int. 50 (2024) 6580–6586.
[12] S. Yu, W. Zhang, L. Li, D. Xu, H. Dong, Y. Jin, Transparent conductive Sb-doped SnO_2/Ag multilayer films fabricated by magnetron sputtering for flexible electronics, Acta Mater. 61 (2013) 5429–5436.
[13] S. Yu, L. Li, W. Zhang, H. Dong, D. Xu, Y. Jin, Transparent conductive Sb-doped SnO_2/Ag multilayer films fabricated by magnetron sputtering for flexible electronics, Vacuum 102 (2014) 43–47.
[14] S. Yu, L. Song, C. Wu, L. Li, Enhanced conductivity and stability of Cu-embedded zinc tin oxide flexible transparent conductive thin films, Ceram. Int. 48 (2022) 15925–15931.
[15] S. Parthiban, E. Elangovan, K. Ramamurthi, R. Martins, E. Fortunato, High near-infrared transparency and carrier mobility of Mo doped In_2O_3 thin films for optoelectronics applications, J. Appl. Phys. 106 (2009) 063716.
[16] M. Grundmann, The Physics of Semiconductors: an Introduction Including Nanophysics and Applications, second ed., Springer, Berlin, Germany, 2010.
[17] T. Dietl, H. Ohno, Dilute ferromagnetic semiconductors: physics and spintronic structures, Rev. Mod. Phys. 86 (2014) 187–251.
[18] J. Liu, M.P. Hanson, J.A. Peters, B.W. Wessels, Magnetism and Mn clustering in (In, Mn)Sb magnetic semiconductors, ACS Appl. Mater. Interfaces 7 (2015) 24159–24167.
[19] S.-C. Chen, C.-H. Wang, H. Sun, C.-K. Wen, C.-F. Lu, C.-L. Tsai, Y.-K. Fu, T.-H. Chuang, Microstructures, electrical and magnetic properties of (Ga, Co)-ZnO films by radio frequency magnetron co-sputtering, Surf. Coating. Technol. 303 (2016) 203–208.
[20] J. Liu, D. Shi, C. Kan, H. Yang, Heat-treatment-induced compositional evolution and magnetic state transition in magnetic chalcogenide semiconductor GeFeTe without structural phase change, ACS Appl. Mater. Interfaces 9 (2017) 38651–38661.
[21] J. Liu, Toward flexible memory application: high-performance phase-change magnetic material Fe: GeTe films realized via quasi-van der Waals epitaxy, J. Mater. Chem. C 10 (2022) 9891–9901.
[22] J. Philip, A. Punnoose, B.I. Kim, K.M. Reddy, S. Layne, J.O. Holmes, B. Satpati, P. R. Leclair, T.S. Santos, J.S. Moodera, Carrier-controlled ferromagnetism in transparent oxide semiconductors, Nat. Mater. 5 (2006) 298–304.
[23] C.-Y. Park, C.-Y. You, K.-R. Jeon, S.-C. Shin, Charge-carrier mediated ferromagnetism in Mo-doped In_2O_3 films, Appl. Phys. Lett. 100 (2012) 222409.
[24] S. Yan, W. Qiao, W. Zhong, C.-T. Au, Y. Dou, Effects of site occupancy and valence state of Fe ions on ferromagnetism in Fe-doped In_2O_3 diluted magnetic semiconductor, Appl. Phys. Lett. 104 (2014) 062404.
[25] B. Tandon, A. Yadav, A. Nag, Delocalized electrons mediated magnetic coupling in Mn−Sn codoped In_2O_3 nanocrystals: plasmonics shows the way, Chem. Mater. 28 (2016) 3620–3624.
[26] X. Luo, L.-T. Tseng, Y. Wang, N. Bao, Z. Lu, X. Ding, R. Zheng, Y. Du, K. Huang, L. Shu, A. Suter, W.T. Lee, R. Liu, J. Ding, K. Suzuki, T. Prokscha, E. Morenzoni, J. B. Yi, Intrinsic or interface clustering-induced ferromagnetism in Fe-doped In_2O_3-diluted magnetic semiconductors, ACS Appl. Mater. Interfaces 10 (2018) 22372–22380.
[27] J. Liu, Manganese-doped transparent conductive magnetic indium oxide films integrated on flexible mica substrates with high mechanical durability, Ceram. Int. 48 (2022) 3390–3396.
[28] J. Liu, Toward flexible X-tronics: transparent conductors with enhanced room-temperature ferromagnetism using Sn–Mn-codoped In_2O_3/mica thin films, Vacuum 205 (2022) 111404.
[29] J.A. Rogers, Z.N. Bao, K. Baldwin, A. Dodabalapur, B. Crone, V.R. Raju, V. Kuck, H. Katz, K. Amundson, J. Ewing, P. Drzaic, Paper-like electronic displays: large-area rubber-stamped plastic sheets of electronics and microencapsulated electrophoretic inks, Proc. Natl. Acad. Sci. USA 98 (2001) 4835.
[30] D. Chen, X. Cui, X. Liu, H. Chen, Bionic gradient flexible fish skin acts as a passive dynamic micro-roughness to drag reduction, Surf. Coating. Technol. 457 (2023) 129337.
[31] Y. Bitla, C. Chen, H.-C. Lee, T.H. Do, C.-H. Ma, L.V. Qui, C.-W. Huang, W.-W. Wu, L. Chang, P.-W. Chiu, Y.-H. Chu, Oxide heteroepitaxy for flexible optoelectronics, ACS Appl. Mater. Interfaces 8 (2016) 32401–32407.
[32] J. Liu, Y. Feng, R. Tang, R. Zhao, J. Gao, D. Shi, H. Yang, Mechanically tunable magnetic properties of flexible $SrRuO_3$ epitaxial thin films on mica substrates, Adv. Electron Mater. 4 (2018) 1700522.
[33] C.-H. Ma, E.-L. Chen, Y.-H. Lai, Y.-C. Chen, L. Chang, Y.-H. Chu, Flexible transparent heteroepitaxial conducting oxide with mobility exceeding 100 $cm^2 V^{-1} s^{-1}$ at room temperature, NPG Asia Mater. 12 (2020) 70.
[34] J. Liu, S. Liu, Y. Wu, Flexible transparent conducting strontium vanadate/mica heteroepitaxial membranes with mechanically tunable transport behaviors, J. Alloys Compd. 895 (2022) 162725.
[35] J. Liu, Flexible correlated $4d^2$ $SrMoO_3$/mica thin films with enhanced optoelectronic performance and high bending stability, Ceram. Int. 49 (2023) 22745–22752.
[36] P.C. Wu, Y.H. Chu, Development of oxide heteroepitaxy for soft technology, J. Mater. Chem. C 6 (2018) 6102–6117.
[37] Y. Zhang, L. Shen, M. Liu, X. Li, X. Lu, L. Lu, C. Ma, C. You, A. Chen, C. Huang, L. Chen, M. Alexe, C.L. Jia, Flexible quasi-two-dimensional $CoFe_2O_4$ epitaxial thin films for continuous strain tuning of magnetic properties, ACS Nano 11 (2017) 8002–8009.
[38] Y. Bitla, Y.-H. Chu, MICAtronics: a new platform for flexible X-tronics, FlatChem 3 (2017) 26–42.
[39] S. Yu, L. Li, X. Lyu, W. Zhang, Preparation and investigation of nano-thick FTO/Ag/FTO multilayer transparent electrodes with high figure of merit, Sci. Rep. 6 (2016) 20399.
[40] S. Yu, L. Zhao, R. Liu, C. Zhang, H. Zheng, Y. Sun, L. Li, Performance enhancement of Cu-based AZO multilayer thin films via graphene fence engineering for organic solar cells, Sol. Energy Mater. Sol. Cells 183 (2018) 66–72.
[41] J.D. Liu, X.S. Miao, F. Tong, W. Luo, Z.C. Xia, Ferromagnetism and electronic transport in epitaxial $Ge_{1-x}Fe_xTe$ thin film grown by pulsed laser deposition, Appl. Phys. Lett. 102 (2013) 102402.
[42] R.K. Gupta, K. Ghosh, S.R. Mishra, P.K. Kahol, Structural, optical and electrical characterization of highly conducting Mo-doped In_2O_3 thin films, Appl. Surf. Sci. 254 (2008) 4018–4023.
[43] A.G. Joshi, D.G. Kuberkar, G.J. Baldha, R.G. Kulkarni, Effect of Mo and Mo-Ca substitution on the superconductivity of $GdBa_2Cu_{3-\delta}$, Physica C 291 (1997) 25–33.
[44] C.-Y. Park, S.-G. Yoon, Y.-H. Jo, S.-C. Shin, Room-temperature ferromagnetism observed in Mo-doped indium oxide films, Appl. Phys. Lett. 95 (2009) 122502.
[45] M. Birkholz, Thin Film Analysis by X-Ray Scattering, first ed., John Wiley & Sons, Weinheim, Germany, 2006.
[46] C.D. Wagner, W.M. Riggs, L.E. Davis, J.F. Moulder, in: G.E. Muilenberg (Ed.), Handbook of X-Ray Photoelectron Spectroscopy, Perkin-Elmer: Eden Prairie, Minnesota, United States of America, 1979.
[47] C. Klingshirn, Semiconductor Optics, second ed., Springer, Germany, 2005.
[48] G. Haacke, New figure of merit for transparent conductors, J. Appl. Phys. 47 (1976) 4086–4089.